INORGANIC CHEMISTRY FRONTIERS

RESEARCH ARTICLE

View Article Online
View Journal | View Issue

Cite this: *Inorg. Chem. Front.*, 2024, **11**, 3820

A highly sensitive Zr-MOF mediated multi-enzyme cascade platform for the colorimetric and fluorescent dual-signal determination of sarcosine†

Nan Wang,[a] Lin Ma,[b] Zhengxuan Li,[b] Chenyu Zhou[a] and Xingguang Su *[a]

Herein, a highly sensitive detection platform for the dual-mode determination of sarcosine by fluorescence and colorimetry was constructed based on zirconium-based metal organic frameworks (Zr-MOFs) with multi-enzyme immobilization. Zr-MOFs with peroxidase-mimicking activity were firstly prepared by a solvothermal method, and sarcosine oxidase (SOX) and horseradish peroxidase (HRP) were simultaneously encapsulated in the Zr-MOFs to form the Zr-MOFs@SOX@HRP composite. Oxidation of sarcosine could be catalyzed by the SOX in the Zr-MOFs@SOX@HRP composite to generate hydrogen peroxide (H_2O_2). The generated H_2O_2 was decomposed through the synergistic catalysis by Zr-MOFs and HRP to generate free radicals that could oxidize the chromogenic substrate *p*-phenylenediamine (PPD) to produce oxPPD. The oxPPD generated could quench the fluorescence of carbon dots at 510 nm *via* the internal filtering effect (IFE). The amount of sarcosine could be sensitively detected by monitoring the changes of the colorimetric and fluorescence signals, with detection limits of 0.44 μM and 0.21 μM, respectively. Thus, the dual-mode detection of sarcosine by fluorescence and colorimetry through a Zr-MOF-mediated cascade reaction system was realized. The method was applied to the determination of sarcosine in the urine of healthy individuals as well as in the urine of prostate cancer patients with satisfactory results, demonstrating its enormous potential for predicting prostate cancer disease.

Received 2nd April 2024,
Accepted 13th May 2024

DOI: 10.1039/d4qi00841c

rsc.li/frontiers-inorganic

1. Introduction

Prostate cancer, the second most common cancer in male patients, is also the fourth most common cancer worldwide.[1–3] Early detection of prostate cancer is usually based on methods such as digital rectal examination, ultrasound in the anorectum, puncture biopsy of the prostate and magnetic resonance imaging. These standard screening methods are invasive and expensive and do not meet the current needs for early screening.[4–6] It is well known that the incidence of cancer has been increasing in recent years and cancer patients are tending to be younger, and the risk of cancer can be significantly reduced if diagnosed and treated at an early stage. For prostate cancer, as one of the most common cancers with the highest incidence rate in male patients, early diagnosis can significantly reduce the mortality rate. Sarcosine (SO), one of the biomarkers of prostate cancer, is a naturally occurring amino acid. When prostate cancer metastasises, the level of sarcosine in the urine of the patient increases significantly. Moreover, sarcosine has been shown to significantly stimulate the growth and metastasis of malignant prostate cells. Therefore, it is extremely necessary to develop efficient, convenient, and sensitive quantitative assays for sarcosine so as to achieve early screening of prostate cancer. Mass spectrometry[7] and electrochemistry[8] methods have been applied to the quantitative determination of sarcosine due to their high accuracy and sensitivity. However, the high cost of these methods and the need for specialized equipment and operators make them difficult to be widely used for early screening.

Fluorescence and colorimetric methods can achieve this goal as a low-cost method, thus contributing to the expansion of cancer screening.[9–12] Wu *et al.* proposed a tetraphenylethene (TPE)-incorporated amorphous nanozyme-based ratiometric fluorescence–colorimetric dual-mode biosensor for achieving the onsite visual detection of hypoxanthine.[13,14] Shen *et al.*[15] developed a novel bimetallic nano-enzyme Fe@CeO_2 with high peroxidase-like activity for the colorimetric detection of hypoxanthine. Attempts have also been made to develop convenient methods to detect sarcosine. Wang *et al.*[16]

[a]*Department of Analytical Chemistry, College of Chemistry, Jilin University, Changchun 130012, China. E-mail: suxg@jlu.edu.cn; Tel: +86-431-85168352*
[b]*State Key Lab of Supramolecular Structure and Materials, College of Chemistry, Jilin University, Changchun, 130012, P. R. China*

† Electronic supplementary information (ESI) available. See DOI: https://doi.org/10.1039/d4qi00841c

established a simple colorimetric method for the determination of sarcosine using gold nanorods. Li *et al.*[17] proposed a MnO_2 nanosheet-mediated cascade reaction system for ratiometric fluorescence detection of sarcosine. Similarly, Wu *et al.*[18] synthesized excitation-dependent fluorescent carbon dots, which were used as fluorescent probes, and 3,3′,5,5′-tetramethylbenzidine (TMB) as a chromogenic substrate for the detection of sarcosine by colorimetric and ratiometric fluorescence methods.

Although the fluorescence and colorimetric methods mentioned above achieve rapid and sensitive sarcosine detection, most of them use bio-enzymes in their assays. Bio-enzymes are preferred for most of the assays due to their low cost, accuracy and specificity, but their instability in non-physiological environments makes them under-utilized and highly consumed in the assay process, limiting their application.[19–21] It has been found that the stability of bio-enzymes could be improved by immobilization of bio-enzymes to prevent problems such as aggregation, autolysis and protein hydrolysis.[22] In addition, immobilization of bio-enzymes has accelerated the substrate consumption and made the reaction more rapid. In the process of immobilization, carriers have a significant impact on the catalytic efficiency of the immobilized bio-enzymes by improving the stability and microenvironment of the bio-enzyme.[23,24] Therefore, the development of carriers is crucial. So far, a variety of carriers with excellent performance have been developed, including various inorganic, organic and composite nanomaterials.[25] Among them, metal–organic frameworks have gradually come into the limelight as carriers for bio-enzymes. Metal–organic frameworks (MOFs) are porous materials self-assembled from a central metal and a ligand with high specific surface area and adjustable pore size, and have the potential to be excellent carriers.[26,27] Hu *et al.* immobilized SOX using a metal–organic framework of the ZIF series to improve stability and established a fluorescence method for the detection of sarcosine. However, although the method immobilized SOX, the HRP used in the system was still in a free state.[28] Gao *et al.* proposed a new strategy for precise construction of micro mesopores to immobilize highly stable hierarchical porous metal–organic framework (HP-Zr-MOF) channel structures for HRP and glucose oxidase, which realized the rapid detection of glucose.[29]

Inspired by the aforementioned studies, as shown in Scheme 1, we utilized Zr-MOFs with peroxidase-like activity to co-encapsulate SOX as well as HRP within the metal–organic framework. And we constructed a fluorescence and colorimetric dual-mode detection strategy by combining the Zr-MOFs@SOX@HRP composite with fluorescent carbon dots (CDs) to monitor sarcosine. The sarcosine oxidase immobilized in Zr-MOFs@SOX@HRP could recognize and oxidize sarcosine to generate H_2O_2 and glycine. The generated H_2O_2 was decomposed by the Zr-MOFs and HRP to generate free radicals, which further oxidized *p*-phenylenediamine (PPD) to generate oxPPD with the absorbance peak at 450 nm. The Zr-MOFs@SOX@HRP could rapidly catalyze the oxidation of PPD due to the synergistic catalytic effects of Zr-MOFs and HRP. The oxPPD generated could quench the fluorescence of the fluorescent carbon dots at 510 nm *via* the internal filtering effect (IFE). Therefore, by monitoring the change of the absorbance and fluorescence signals in the system, a colorimetric and fluorescence dual-signal detection platform for the determination of sarcosine was established for the first time.

2. Experimental section

2.1 Reagents and instruments

Detailed descriptions of the reagents and instruments are provided in the ESI.†

2.2 The synthesis of the Zr-MOFs@SOX@HRP composite

Zr-MOFs were prepared according to a facile one-step approach with minor modifications.[30] Zirconium chloride (27 mg) was dissolved in 10 mL of DMF, and 2,2′-bipyridine-5,5′-dicarboxylic acid (bpydc, 80 mg) was dispersed in 10 mL of DMF. Then, after the two reactants were mixed well, 500 μL acetic acid was added to the above mixed solution. The mixture was sonicated for 30 min and heated at 90 °C for 18 h. The white product was washed three times with DMF and THF, respectively, centrifuged and dried under vacuum. The Zr-MOF (40 mg) prepared above were added to a SOX (5 mL, 2 mg mL^{-1}) and HRP (5 mL, 1 mg mL^{-1}) solution, and incubated for 40 min at 40 °C. After that, the Zr-MOFs@SOX@HRP composite was collected by centrifugation and washed with water 3 times, and placed in the refrigerator at 4 °C for further use.

2.3 Fluorometric and colorimetric detection of sarcosine

The method for the synthesis of fluorescent carbon dots is provided in the ESI.† For the detection of sarcosine, a series of sarcosine solutions (100 μL) at different concentrations, Tris-HCl buffer solution (100 μL, 0.1 M, pH 8.9), Zr-MOFs@SOX@HRP (20 μL, 1 mg mL^{-1}) and PPD (100 μL, 10 mM) were mixed, diluted to 1.0 mL with ultrapure water, mixed well and reacted for 40 min at 45 °C. After adding the above solution to fluorescent carbon dots (50 μL) and reacting for 1 min the UV-Vis absorption spectra were obtained in the range of 350–700 nm. The fluorescence spectra were collected in the range of 380–700 nm (Ex = 360 nm).

2.4 Sarcosine assay in human urine samples

Urine samples from healthy individuals and prostate cancer patients were provided by Changchun Sino-Japanese United Hospital and were frozen and preserved for use. Urine samples were filtered through an ultrafiltration membrane and centrifuged at 10 000 rpm for 10 min. Thereafter, a series of spiked samples were prepared by mixing the urine with sarcosine at various concentrations (10, 60 and 100 μM). The procedure for sarcosine analysis was the same as the above procedure in section 2.3.

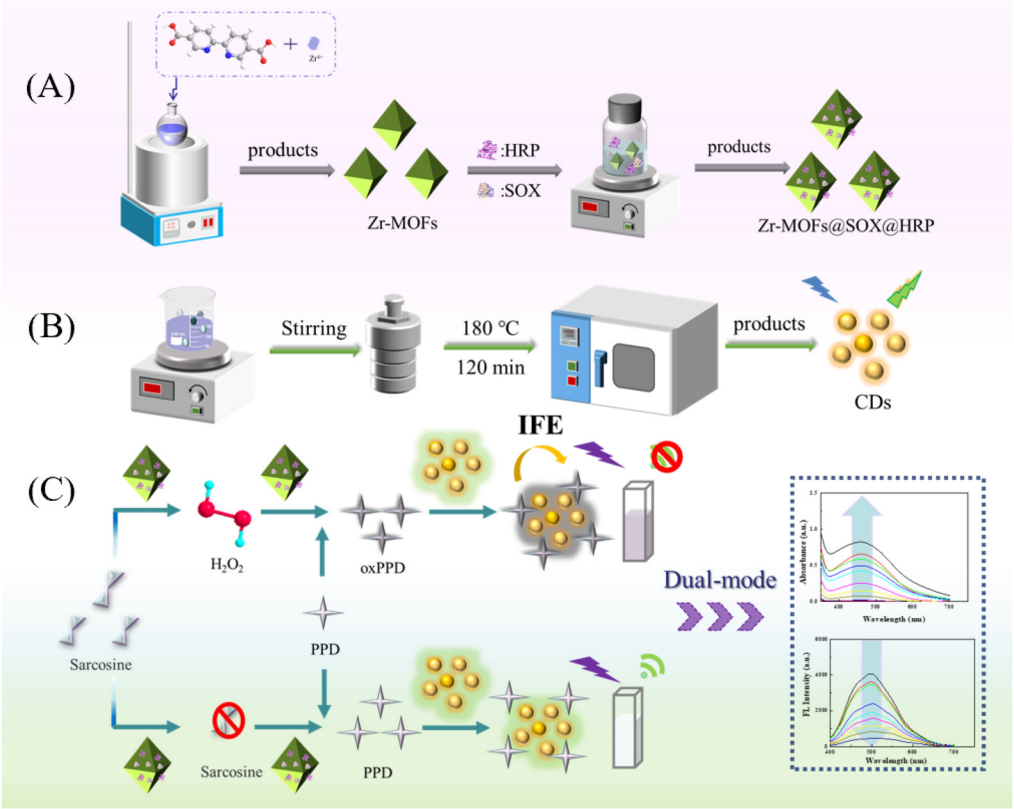

Scheme 1 Schematic diagram of the synthesis of Zr MOFs@SOX@HRP (A) and CDs (B). (C) The mechanism diagram of fluorescence and colorimetric dual-signal detection of sarcosine.

3. Results and discussion

3.1 Characterization of Zr-MOFs@SOX@HRP

The synthesis of the Zr-MOFs@SOX@HRP composite is shown in Scheme 1(A). Zr-MOFs were synthesized from zirconium chloride and bpydc as precursor materials. The TEM images (Fig. 1(A) and (B)) show that the synthesized Zr-MOFs had a bipyramidal structure with a particle diameter of about 150 nm. The Zr-MOFs@SOX@HRP composite was synthesized based on the Zr-MOFs, and the synthesis process was optimized to obtain the best performance. As can be seen from Fig. S1–S4,† the Zr-MOFs@SOX@HRP composite was synthesized optimally when the ratio of HRP to SOX was 1 : 2, the reaction temperature was 40 °C, the reaction time was 40 min, and the concentration of Zr-MOFs was 4 mg mL^{-1}. The morphology of the Zr-MOFs@SOX@HRP composite was also explored by TEM. The TEM images (Fig. 1(C) and (D)) clearly indicated that the morphology of the Zr-MOFs@SOX@HRP was similar to that of Zr-MOFs. To better identify SOX and HRP immobilized in the Zr-MOFs, validation was performed by CLSM images. Co-immobilization of FITC-labeled SOX and RhB-labeled HRP in the Zr-MOFs could be clearly seen in the CLSM images (Fig. 1(E)–(H)). And in the XRD pattern (Fig. 1 (I)), the characteristic (111) and (200) peaks of the Zr-MOFs@SOX@HRP composite were consistent with those of pure Zr-MOFs. The peak intensities of the Zr-MOFs@SOX@HRP composite were significantly lower compared with those of the pure Zr-MOFs, which was attributed to the fact that SOX and HRP occupied some of the sites of the Zr-MOFs, resulting in lower crystallinity than that of the pure Zr-MOFs. FT-IR spectra also further verified the encapsulation of SOX and HRP. The band at 1644 cm^{-1} corresponding to protein amide I was also observed for the Zr-MOFs@SOX@HRP composite (Fig. 1(J)), suggesting that SOX and HRP were successfully embedded in the Zr-MOFs.[31] The elemental composition of the Zr-MOFs@SOX@HRP composite were further verified using X-ray photoelectron spectroscopy (XPS) experiments. As shown in Fig. 1(K), the XPS full spectrum clearly displays the presence of six main peaks at 284.8, 333.0, 182.4, 399.6, 531.4 and 721.6 eV for C 1s, Zr 3p, Zr 3d, N 1s, O 1s and Fe 2p, respectively.

The stability of nanomaterials is the basis for the construction of highly stable detection platforms. Therefore, the stability of the Zr-MOFs@SOX@HRP composite was investigated. In the temperature stability study, there was almost no effect on the activity of the Zr-MOFs@SOX@HRP composite under the conditions of −20 °C to 60 °C (Fig. S5†). Moreover, Zr-MOFs@SOX@HRP maintained high catalytic activity in weakly acidic, neutral and alkaline environments (Fig. S6†). In addition, Zr-MOFs@SOX@HRP also showed excellent stability under high salt concentration storage (Fig. S7†).

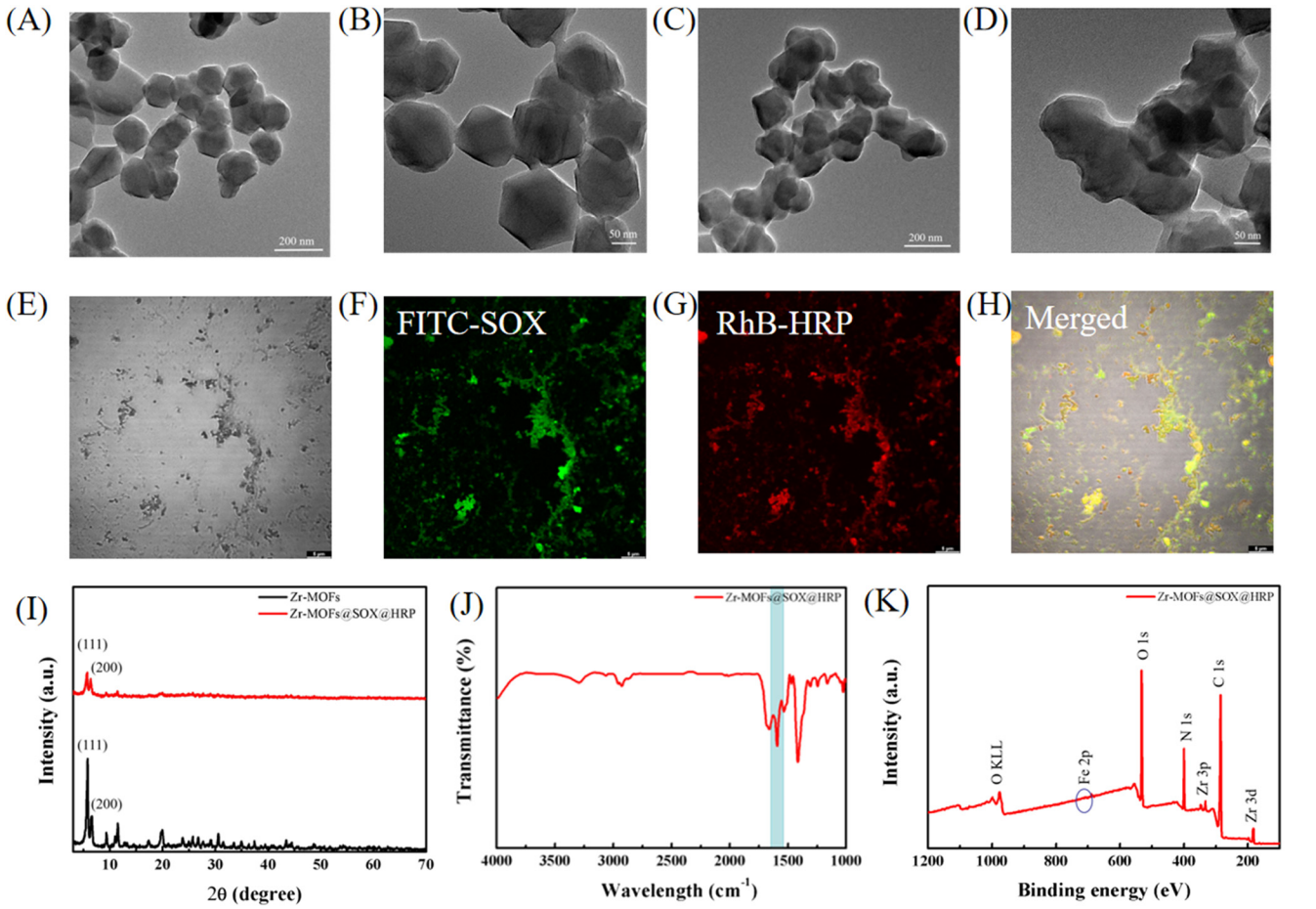

Fig. 1 (A and B) TEM images of Zr-MOFs. (C and D) TEM images of Zr-MOFs@SOX@HRP. (E) Optical image of Zr-MOFs@FITC-SOX@RhB-HRP. CLSM dark field images of FITC-SOX (F), RhB-HRP (G), and a merged image (H). (I) The XRD patterns of Zr-MOFs and Zr-MOFs@SOX@HRP. (J) The FTIR spectrum of Zr-MOFs@SOX@HRP. (K) The XPS spectrum of Zr-MOFs@SOX@HRP.

3.2 The catalysis mechanism and enzyme-like activity of Zr-MOFs@SOX@HRP

The catalytic activity of the encapsulated HRP was monitored by catalytic oxidation of the chromogenic substrate 3,3′,5,5′-tetramethylbenzidine (TMB) in the presence of H_2O_2 (Fig. 2(A)). As displayed in Fig. 2(B), when TMB was not oxidized, there was no absorption peak at 652 nm. When H_2O_2 co-existed with TMB, TMB could not be oxidized, thus there was also no absorption peak at 652 nm. As shown in Fig. 2(B), the free HRP and Zr-MOFs both produced an absorption peak at 652 nm in the presence of H_2O_2 and TMB, and the color change is shown in the inset. When H_2O_2 and TMB were present in the Zr-MOFs@SOX@HRP solution simultaneously, a more obvious color change could be observed, and the absorption intensity at 652 nm was significantly stronger than that of free HRP and Zr-MOFs, so the enhanced catalytic ability of Zr-MOFs@SOX@HRP was due to synergistic catalysis effects of Zr-MOFs and HRP.[32–34] Meanwhile, Fig. 2(C) further shows that the absorbance intensity at 652 nm increased with increasing reaction time for Zr-MOFs@SOX@HRP. Free radical scavenging experiments were performed to determine the types of free radicals generated during the catalytic process with Zr-MOFs@SOX@HRP. As shown in Fig. 2(D), the absorbance intensity at 652 nm decreased significantly with the addition of *p*-BQ, and the degree of the decrease in absorbance was greater with the increase in the concentration of *p*-BQ. This indicated that $O_2^{\bullet-}$ was generated during the catalytic process. Furthermore, the presence of $^{\bullet}OH$ was verified by the reaction of non-fluorescent terephthalic acid (TA) with $^{\bullet}OH$ to produce fluorescent products. As shown in Fig. 2(E), when Zr-MOFs@SOX@HRP was added to the TA/H_2O_2 system, a clear fluorescence peak appeared at 426 nm, and the larger TA concentration produced a fluorescence peak with higher intensity, which indicated that $^{\bullet}OH$ was also produced in the catalysis process.

3.3 Characterization of fluorescent carbon dots

The morphology of the prepared fluorescent carbon dots was analyzed by TEM. Fig. 3(A) shows that the synthesized CDs had a spherical structure and the particle size was around 2.5 nm (Fig. 3(B)). FT-IR spectroscopy was carried out to determine the functional groups of the CDs. As shown in Fig. S8,†

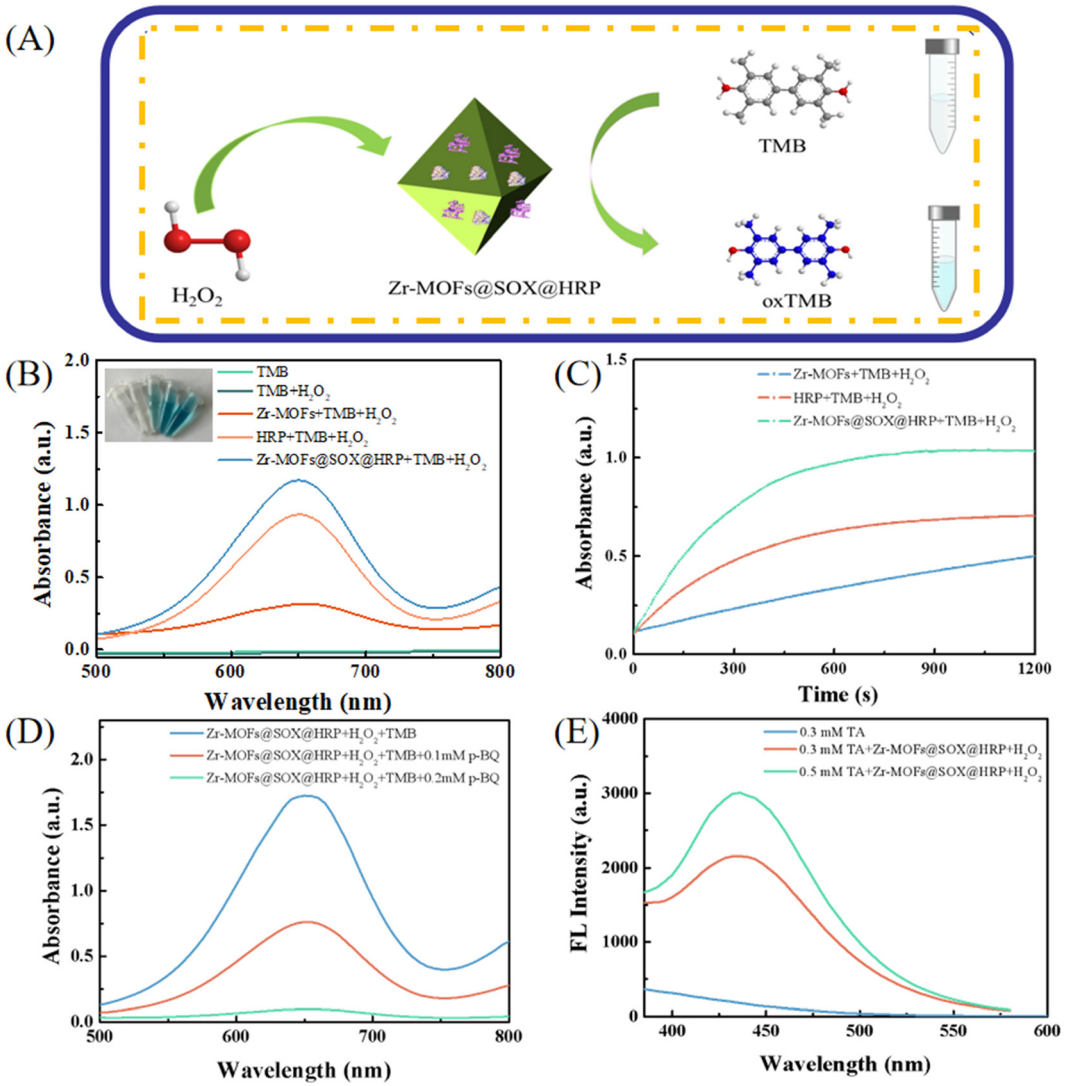

Fig. 2 (A) Schematic illustration of TMB oxidation catalyzed by Zr-MOFs@SOX@HRP. (B) UV-vis absorption spectra of TMB, TMB + H_2O_2, Zr-MOFs + TMB + H_2O_2, HRP + TMB + H_2O_2, and Zr-MOFs@SOX@HRP + TMB + H_2O_2. (C) Absorbance curves of Zr-MOFs/TMB/H_2O_2, HRP/TMB/H_2O_2 and Zr-MOFs@SOX@HRP/TMB/H_2O_2 with time. (D) UV-vis absorption spectra of the Zr-MOFs@SOX@HRP/H_2O_2/TMB system with different concentrations of *p*-BQ. (E) Fluorescence emission spectra of 0.3 mM TA, 0.3 mM TA + H_2O_2 + Zr-MOFs@SOX@HRP and 0.5 mM TA + H_2O_2 + Zr-MOFs@SOX@HRP.

the FT-IR spectrum revealed the presence of hydroxyl and amino asymmetric stretching vibrations at 3325 cm^{-1} and 3203 cm^1. The characteristic absorption bands at 1514 cm^{-1} and 1138 cm^{-1} belonged to the C=N and C–O stretching vibrations.[35] This indicated that abundant hydroxyl and amino groups were present on the CDs. The elemental composition and bonding of the CDs were characterized using XPS. The XPS spectra revealed that C, N and O elements were the constituent elements of the CDs (Fig. 3(C)). As shown in Fig. 3(D), the spectrum of carbon 1s displayed three fitted peaks at 284.4, 285.1 and 285.9 eV attributed to the C–C/C=C, C–N and C–O bonds. The spectrum of N 1s displayed two fitted peaks at 399.8 eV and 398.9 eV, which were attributed to pyridine nitrogen and pyrrolic nitrogen (Fig. 3(E)). As displayed in Fig. 3(F), the O 1s spectrum was split into two well-resolved parts at 531.4 eV and 530.7 eV, corresponding to C–O and C=O, respectively.[36] The fluorescence properties of the CDs were investigated by fluorescence spectroscopy. The maximum excitation wavelength and emission wavelength of the CDs were 360 nm and 510 nm, respectively (Fig. 3(G)). As depicted in Fig. 3(H), the emission wavelength of the CDs hardly changed during the change of the excitation wavelength from 340 nm to 400 nm, exhibiting no excitation-dependent properties. Meanwhile, the fluorescence colors of the CDs were also marked on a CIE plot (Fig. 3(I)), and they were in the green region. Afterward, the stability of the CDs was also explored. As shown in Fig. S9 and S10,† the fluorescence intensity of CDs stored at −20 °C to 60 °C and in high salt concentration environments had almost no obvious change. As depicted in Fig. S11,† it could be noticed that the fluorescence intensity of

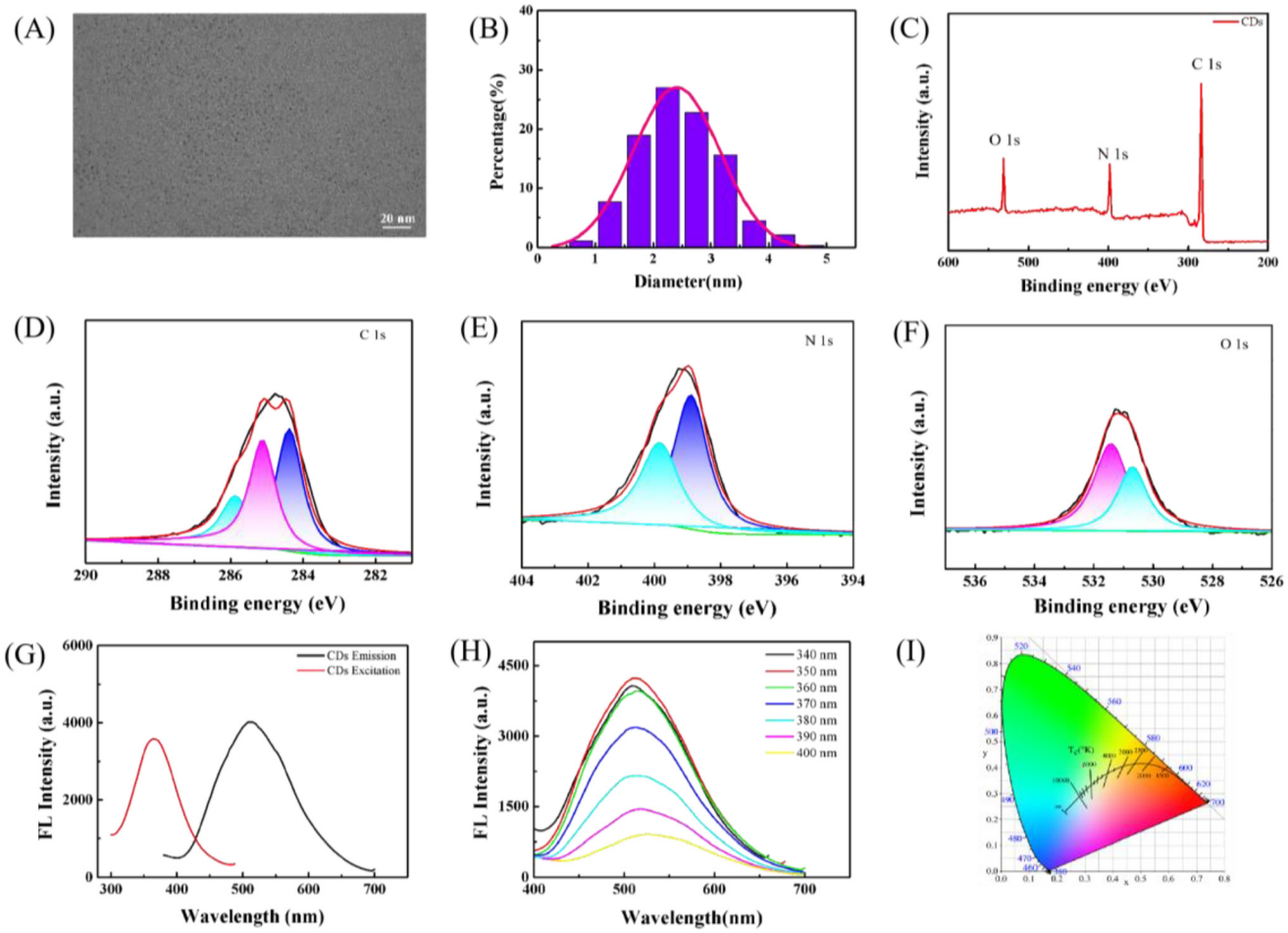

Fig. 3 (A) TEM images of CDs. (B) The size distribution of CDs. (C) XPS spectra of CDs. (D) XPS analysis of C 1s of CDs. (E) XPS analysis of N 1s of CDs. (F) XPS analysis of O 1s of CDs. (G) The excitation (Ex) and emission (Em) spectra of CDs. (H) Fluorescence emission spectra under excitation wavelengths from 340 to 400 nm. (I) The CIE chromaticity coordinates of CDs.

the CDs was almost unchanged in acidic and neutral environments, and there was a slight decrease in fluorescence intensity in strong alkaline environments. The good photostability of the CDs was also verified by the unchanged fluorescence intensity of the CDs after 1 h of xenon lamp irradiation (Fig. S12†). The above results suggested that the synthesized CDs were stable and had the potential to be used in detection platforms.

3.4 Construction of a fluorescence and colorimetric dual-signal detection platform for sarcosine

As shown in the schematic diagram in Fig. 4(A), a dual-signal detection platform for sarcosine based on Zr-MOFs@SOX@HRP and CDs was successfully constructed. The promoted cascade enzyme activity was attributed to SOX and HRP being immobilization in the Zr-MOFs, and the proximity of sarcosine triggered a substrate channeling effect, which resulted in shorter diffusion paths and rapid intermediate/substrate depletion as compared to the free enzyme system. Due to the higher catalytic efficiency of sarcosine oxidase in alkaline environments, and among the many chromogenic substrates, *p*-phenylenediamine (PPD) was more stable in alkaline environments compared to other substrates. Therefore, PPD was chosen as a chromogenic substrate in the detection system. As shown in Fig. 4(B), when sarcosine was present in the Zr-MOFs@SOX@HRP/PPD system, the absorbance peak of oxPPD at 450 nm increased significantly. In addition, it was clearly observed that the PPD solution was colourless and brown when oxPPD was formed by oxidation (Fig. S13†). When CDs were added to the above system, a decrease in their fluorescence intensity at 510 nm was clearly observed (Fig. 4(C)). The mechanism of the above detection platform for sarcosine determination was further validated. As cab be seen in Fig. 4 (D), the emission spectrum of CDs and the absorption spectrum of oxPPD had great overlap. Fig. S14† shows that the absorption spectrum of the CDs/oxPPD system was similar to that of the direct theoretical sum of the absorption spectra of the CDs and oxPPD, implying there was no interaction or ground-state complex formation between CDs and oxPPD. Subsequently, we measured the fluorescence lifetimes of the

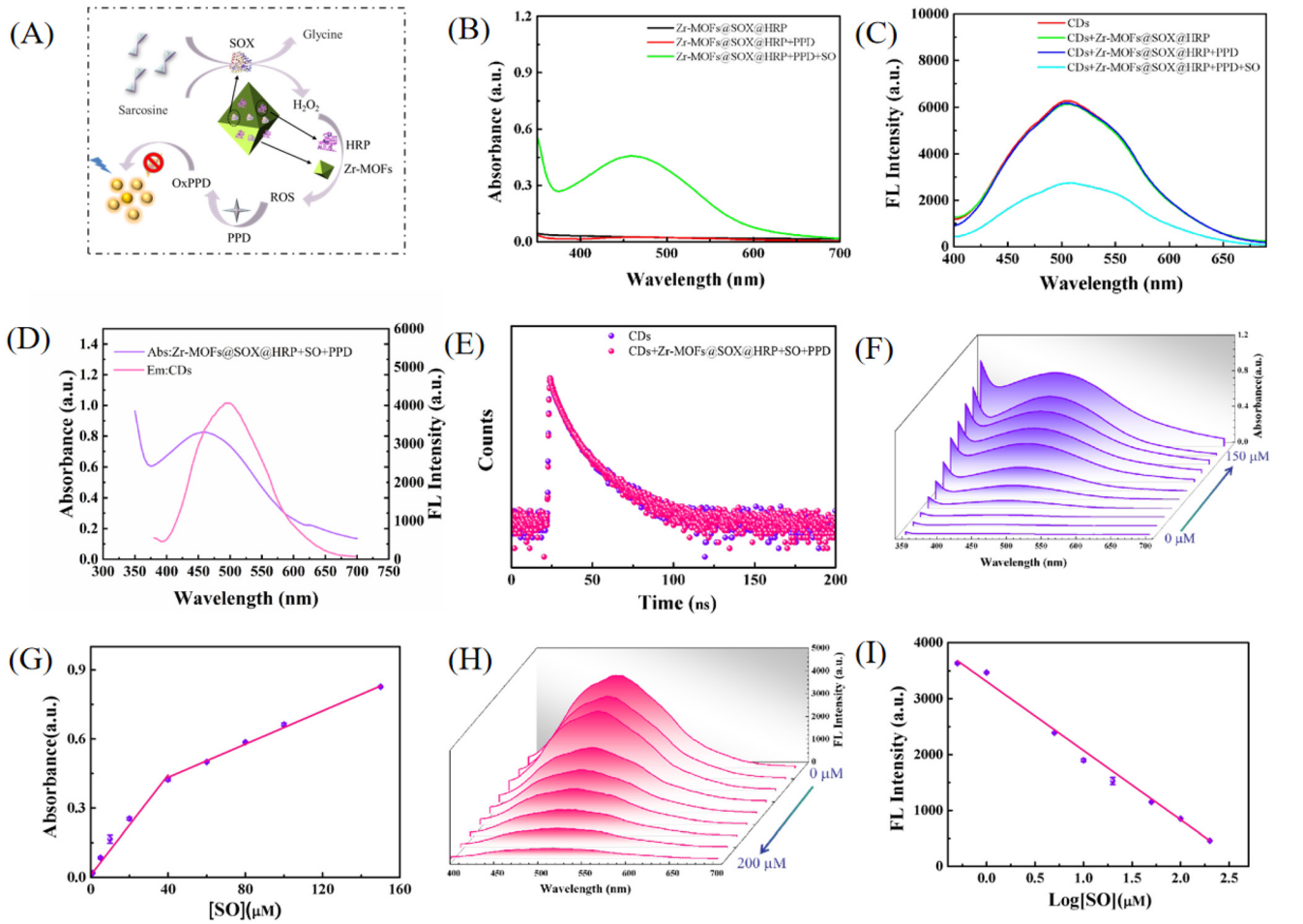

Fig. 4 (A) The schematic diagram of the dual-signal detection platform for sarcosine. (B and C) Feasibility of sarcosine analysis. (D) UV-vis absorption spectrum of Zr-MOFs@SOX@HRP + SO + PPD and fluorescence emission spectrum of CDs. (E) Fluorescence lifetime of the CDs and CDs/Zr-MOFs@SOX@HRP/PPD. (F) UV-vis absorption spectra of Zr-MOFs@SOX@HRP/PPD system with various concentrations of sarcosine. (G) The standard curve of absorbance at 450 nm *versus* concentration of sarcosine. (H) Fluorescence emission spectra of the CDs/Zr-MOFs@SOX@HRP/PPD system with various concentrations of sarcosine. (I) The standard curve of fluorescence intensity at 510 nm *versus* logarithmic concentration of sarcosine.

CDs and the CDs/Zr-MOFs@SOX@HRP/PPD system, which were 7.61 ns and 7.60 ns, respectively (Fig. 4(E)). The above results indicated that it was the IFE effect that caused the fluorescence quenching of the CDs.

The pivotal factors of incubation pH, incubation time and incubation temperature for the catalytic reaction between Zr-MOFs@SOX@HRP and sarcosine were explored to construct a sensitive and stable dual-mode analysis system for sarcosine detection. As shown in Fig. S15–S17,† the optimal incubation time, pH and incubation temperature for this detection platform were 40 min, pH 8.9 and 45 °C, respectively. In addition, the reaction time of CDs with Zr-MOFs@SOX@HRP/PPD was optimized. As displayed in Fig. S18,† the oxPPD generated in the detection system could quickly quench the fluorescence of carbon dots within 1 min, and the reaction time of 1 min was finally chosen for the fluorescence assay. Under the optimized conditions, as displayed in Fig. 4(F), the absorbance at 450 nm increased significantly with the increase in the concentration of sarcosine. The absorption intensity displayed a good linear relationship with sarcosine concentration in the ranges of 0.5–40 μM and 40–150 μM. The regression equations were I = 0.0096 + 0.0108[sarcosine] (μM, R^2 = 0.989) and I = 0.2884 + 0.0036[SO] (μM, R^2 = 0.997), respectively (Fig. 4(G)). The decrease in the slope could be attributed to kinetic limitations.[37] Calculated by the equation LOD = $3\sigma/k$, the LOD of sarcosine was 0.44 μM. And the LOQ of sarcosine was 1.45 μM. As shown in Fig. 4(H), the fluorescence intensity of the CDs decreased with the increase of sarcosine concentration, with a good linear relationship in the range of 0.5–200 μM. The regression equation was F = 3310 − 1238.5log[sarcosine] (μM, R^2 = 0.998) (Fig. 4(I)), with a LOD value of 0.21 μM. Furthermore, the LOQ of sarcosine was 0.69 μM. The relative standard deviation for 0.5 μM sarcosine detection in six replicates is lower than 4.67%, which indicates the good repeatability of the methodology. As depicted in Table S1,† the dual-signal detection platform based on Zr-MOFs@SOX@HRP and

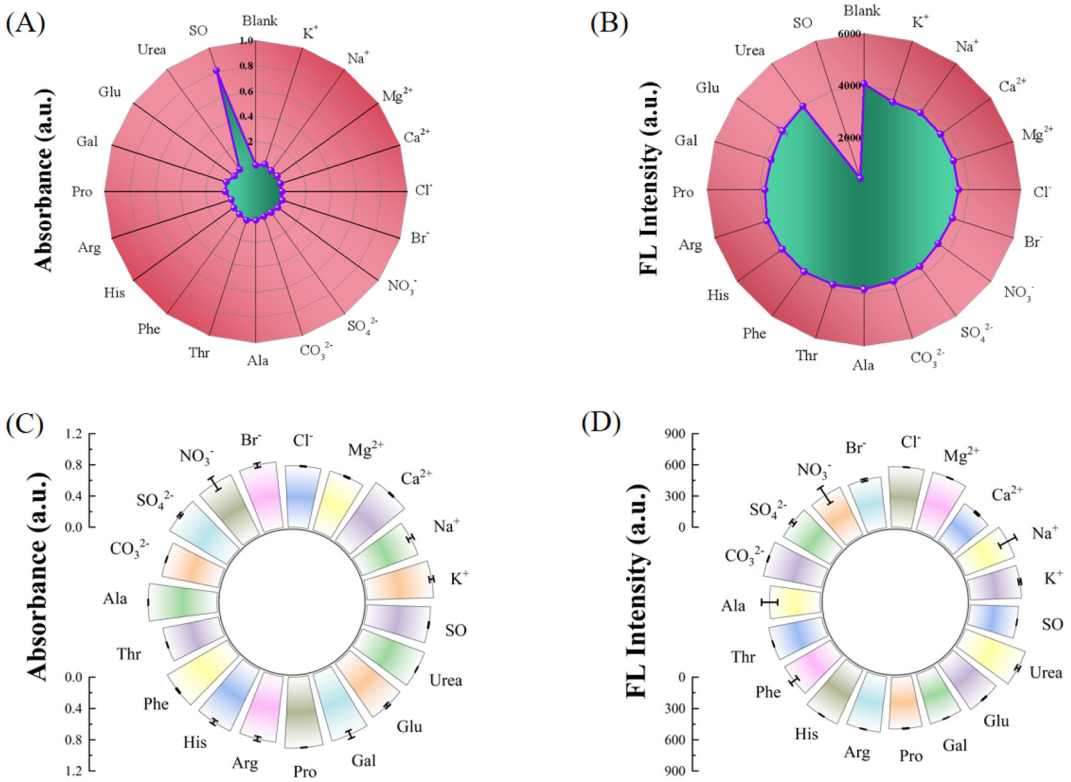

Fig. 5 Selectivity of the colorimetric (A) and fluorescence (B) dual-signal detection platform for sarcosine. Anti-interference ability for the colorimetric (C) and fluorescence (D) dual-signal detection platform for sarcosine.

CDs was constructed for the first time for the detection of sarcosine, and the sensitivity of this detection platform was satisfactory compared with other methods. In addition, Table S1† shows that our method had a comparable range of quantification, and these results suggest the potential of this dual-signal detection platform for the diagnosis of prostate cancer.

3.5 Analytical performance of the sarcosine assay

In order to examine the anti-interference ability and selectivity of the detection platform, some ions, amino acids, and sugars as well as urea commonly contained in urine were added to the detection platform. As shown in Fig. 5(A) and (B), only when sarcosine was added to the system was there a change in the absorption intensity at 450 nm as well as the fluorescence intensity at 510 nm. Meanwhile, as shown in Fig. 5(C) and (D), when sarcosine coexisted with the above interfering substances in the system, they did not affect its specific response to sarcosine. The above results demonstrated that the dual-signal detection platform based on Zr-MOFs@SOX@HRP and CDs had good selectivity for sarcosine detection.

3.6 Sarcosine analysis in urine samples

The developed dual-signal detection platform was applied to the determination of urine from healthy individuals and prostate cancer patients. The spiked urine samples with different concentrations of sarcosine (10, 60 and 100 μM) were also determined and the spiked recoveries were calculated (see Table 1). The results demonstrated that the spiked recoveries

Table 1 The results for sarcosine detection in urine samples

		Colorimetric			Fluorometric		
Sample	Spiked (μM)	Found (μM)	Recovery (%)	RSD (n = 3,%)	Found (μM)	Recovery (%)	RSD (n = 3,%)
Healthy individuals	0	—	—	—	—	—	—
	10	10.13	101.30	0.92	9.73	97.30	1.50
	60	59.30	98.80	0.78	60.10	100.17	1.82
	100	103.07	103.07	1.20	99.00	99.00	3.75
Prostate cancer patients	0	3.14	—	—	3.19	—	—
	10	13.28	101.40	2.83	13.61	104.20	3.54
	60	64.15	101.68	1.41	63.20	100.20	1.84
	100	102.93	99.79	2.12	103.09	99.90	0.78

of sarcosine were in the range of 97.30%–104.20%, with relative standard deviations (RSDs) of 0.78–3.75%. These results indicated that the fluorescence and colorimetric dual-signal detection platform had great potential in the quantitative determination of sarcosine in complex samples.

4. Conclusion

In summary, a facile method for the synthesis of compartmentally immobilized sarcosine oxidase and HRP in Zr-MOFs with peroxidase-mimicking activity under mild conditions was reported. And a dual-signal colorimetric and fluorescence method based on Zr-MOFs@SOX@HRP and CDs was established for sensitively monitoring sarcosine. With the synergistic catalytic effect of Zr-MOFs and HRP and the Zr-MOFs-mediated cascade reaction system, the sensitivity of both fluorescence detection and colorimetric detection is greatly improved. The designed sensor not only overcomes the disadvantage of the instability of free bio-enzymes in the system, but also the dual-signal readout mode has complementary advantages, which improves the analytical accuracy of the biosensor and its practical application.

Conflicts of interest

There are no conflicts to declare.

Acknowledgements

This work is supported by the National Natural Science Foundation of China (No. 22374058, 21775052), and the Open Funds of the State Key Laboratory of Electroanalytical Chemistry, China (No. SKLEAC202201).

References

1 T. Zhu, Q. Tang, Y. Zeng, S. Chen, Y. Yang, H. Wang, J. Chen, L. Guo and L. Li, Sensitive determination of prostate-specific antigen with graphene quantum dot-based fluorescence aptasensor using few-layer V_2CTx MXene as quencher, *Spectrochim. Acta, Part A*, 2023, **293**, 122474.

2 R. L. Siegel, K. D. Miller, H. E. Fuchs and A. Jemal, Cancer Statistics, *Ca-Cancer J. Clin.*, 2021, **1**, 7–33.

3 A. Sreekumar, L. M. Poisson, T. M. Rajendiran, A. P. Khan, Q. Cao, J. D. Yu, B. Laxman, R. Mehra, R. J. Lonigro, Y. Li, M. K. Nyati, A. Ahsan, S. Kalyana-Sundaram, B. Han, X. H. Cao, J. Byun, G. S. Omenn, D. Ghosh, S. Pennathur, D. C. Alexander, A. Berger, J. R. Shuster, J. T. Wei, S. Varambally, C. Beecher and A. M. Chinnaiyan, Metabolomic profiles delineate potential role for sarcosine in prostate cancer progression, *Nature*, 2009, **457**, 910–914.

4 G. Gkotsos, C. Virgiliou, I. Lagoudaki, C. Sardeli, N. Raikos, G. Theodoridis and G. Dimitriadis, The role of sarcosine, uracil, and kynurenic acid metabolism in urine for diagnosis and progression monitoring of prostate cancer, *Metabolites*, 2017, **7**, 1.

5 X. Filella and L. Foj, Prostate Cancer Detection and Prognosis: From Prostate Specific Antigen (PSA) to Exosomal Biomarkers, *Int. J. Mol. Sci.*, 2016, **17**, 1784.

6 T. Yogo, K. Umezawa, M. Kamiya, R. Hino and Y. Urano, Development of an Activatable Fluorescent Probe for Prostate Cancer Imaging, *Bioconjugate Chem.*, 2017, **28**, 2069–2076.

7 T. E. Meyer, S. D. Fox, H. J. Issaq, X. Xu, L. W. Chu, T. D. Veenstra and A. W. Hsing, A Reproducible and High-Throughput HPLC/MS Method To Separate Sarcosine from α- and β-Alanine and To Quantify Sarcosine in Human Serum and Urine, *Anal. Chem.*, 2011, **83**, 5735–5740.

8 M. J. Pannell, E. E. Doll, N. Labban, M. B. Wayu, J. A. Pollock and M. C. Leopold, Versatile sarcosine and creatinine biosensing schemes utilizing layer-by-layer construction of carbon nanotube-chitosan composite films, *J. Electroanal. Chem.*, 2018, **814**, 20–30.

9 J. Mandal, P. Ghorai, P. Brandão, K. Pal, P. Karmakar and A. Saha, An aminoquinoline based biocompatible fluorescent and colourimetric pH sensor designed for cancer cell discrimination, *New J. Chem.*, 2018, **42**, 19818–19826.

10 N. H. Moghadam, S. Salehzadeh, J. Rakhtshah, H. Tanzadehpanah, A. H. Moghadam, F. Hajibabaei, S. Sharifinia, S. S. Asl and M. Saidijam, Improving antiproliferative effect of the nevirapine on Hela cells by loading onto chitosan coated magnetic nanoparticles as a fully biocompatible nano drug carrier, *Int. J. Biol. Macromol.*, 2018, **118**, 1220–1228.

11 S. Anbu, A. Paul, K. Surendranath, A. Sidali and A. J. L. Pombeiro, Naphthalimide-phenanthroimidazole incorporated new fluorescent sensor for "turn-on" Cu^{2+} detection in living cancer cells, *J. Inorg. Biochem.*, 2021, **220**, 111466.

12 A. Elaissi, E. Elsharkawy, R. El Mokni, H. Debbabi, V. Brighenti, S. Nardoni, F. Pellati and S. Hammami, Chemical composition, antifungal and antiproliferative activities of essential oils from Thymus numidicus L, *Nat. Prod. Res.*, 2020, **35**, 5888–5893.

13 G. Wu, J. Luo, C. Du, Z. Zheng, Y. Zhang, P. Luo, Y. Wu and Y. Shen, AIE fluorescent nanozyme-based dual-mode biosensor for analysis of the bioactive component hypoxanthine in meat products, *Food Chem.*, 2024, **450**, 139242.

14 G. Wu, H. Qiu, X. Lin, P. Luo, Y. Wu and Y. Shen, Nanomaterials-based fluorescent assays for pathogenic bacteria in food-related matrices, *Trends Food Sci. Technol.*, 2023, **142**, 104214.

15 G. Wu, A. Dilinaer, P. Nie, X. Liu, Z. Zheng, P. Luo, W. Chen, Y. Wu and Y. Shen, Dual-modal bimetallic nanozyme-based sensing platform combining colorimetric and photothermal signal cascade catalytic enhancement for detection of hypoxanthine to judge meat freshness, *J. Agric. Food Chem.*, 2023, **71**, 16381–16390.

16 Q. Zhong, X. Qin, C. Yuan, R. Shi and Y. Wang, Colorimetric determination of sarcosine in human urine

with enzyme-like reaction mediated Au nanorods etching, *Microchem. J.*, 2021, **165**, 106120.
17 W. Li, T. Li, S. Chen, D. Deng, Y. Ji and R. Li, Nanozyme-mediated cascade reaction system for ratiometric fluorescence detection of sarcosine, *Sens. Actuators, B*, 2022, **355**, 131341.
18 W. Qin, H. Tian, Z. Meng, Z. Tang, J. Wang and Z. Wu, Facile synthesis and ozonation of carbon dots using mango pulps for dual-mode colorimetry and ratiometric fluorescence detection of sarcosine, *Microchem. J.*, 2023, **195**, 109468.
19 R. J. Taylor, M. B. Geeson, T. Journeaux and G. J. L. Bernardes, Chemical and Enzymatic Methods for Post-Translational Protein–Protein Conjugation, *J. Am. Chem. Soc.*, 2022, **144**, 14404–14419.
20 S. Yamaura, S.-i. Sakasegawa, E. Koguma, S. Ueda, Y. Kayamori, D. Sugimori and K. Karasawa, Novel enzymatic method for assaying Lp-PLA 2 in serum, *Clin. Chim. Acta*, 2018, **481**, 184–188.
21 R. Paleari, G. Bonetti, C. Callà, M. Carta, F. Ceriotti, N. Di Gaetano, M. Ferri, E. Guerra, G. Lavalle, C. L. Cascio, F. G. Martino, M. Montagnana, M. Moretti, G. Santini, D. Scribano, R. Testa, A. Vero and A. Mosca, Multicenter evaluation of an enzymatic method for glycated albumin, *Clin. Chim. Acta*, 2017, **469**, 81–86.
22 W. Xu, L. Jiao, H. Yan, Y. Wu, L. Chen, W. Gu, D. Du, Y. Lin and C. Zhu, Glucose Oxidase-Integrated Metal-Organic Framework Hybrids as Biomimetic Cascade Nanozymes for Ultrasensitive Glucose Biosensing, *ACS Appl. Mater. Interfaces*, 2019, **11**, 22096–22101.
23 X. Xiang, H. Pang, T. Ma, F. Du, L. Li, J. Huang, L. Ma and L. Qiu, Ultrasound targeted microbubble destruction combined with Fe-MOF based bio-/enzyme-mimics nanoparticles for treating of cancer, *J. Nanobiotechnol.*, 2021, **19**, 1.
24 Q. Wang, X. Zhang, L. Huang, Z. Zhang and S. Dong, GOx@ZIF–8(NiPd) Nanoflower: An Artificial Enzyme System for Tandem Catalysis, *Angew. Chem., Int. Ed.*, 2017, **56**, 16082–16085.
25 N. Li, H. Yin, J. Pei, Y. Huang, G. Xu, H. Yuan, X. Liu and Y. Yang, A Novel Ship-in-Bottle Type Immobilized HRP via Co-adsorption of Super Paramagnets and HRP into Silica Hollow Fiber, *J. Inorg. Organomet. Polym. Mater.*, 2017, **28**, 751–766.
26 H. Cheng, L. Zhang, J. He, W. Guo, Z. Zhou, X. Zhang, S. Nie and H. Wei, Integrated Nanozymes with Nanoscale Proximity for in Vivo Neurochemical Monitoring in Living Brains, *Anal. Chem.*, 2016, **88**, 5489–5497.
27 B. Zhang, X. Li, W. Shu, Y.-S. Yang, H.-L. Zhu and C. Shao, A self-supplied O_2 versatile nanoplatform for GOx-mediated synergistic starvation and hypothermal photothermal therapy, *Mater. Des.*, 2022, **222**, 111067.
28 Q. Hu, G. Chen, L. Wang, X. Cui, C. Chang and Q. Fu, Nanoreactor of sarcosine oxidase-embedded ZIFs activates fluorescent response for diagnosis of prostate cancer, *New J. Chem.*, 2022, **46**, 8912–8918.
29 H. Liu, Y. Du, J. Gao, L. Zhou, Y. He, L. Ma, G. Liu, Z. Huang and Y. Jiang, Compartmentalization of Biocatalysts by Immobilizing Bienzyme in Hollow ZIF-8 for Colorimetric Detection of Glucose and Phenol, *Ind. Eng. Chem. Res.*, 2019, **59**, 42–51.
30 W. H. Chen, M. Vázquez-González, A. Kozell, A. Cecconello and I. Willner, Cu^{2+}–Modified Metal-Organic Framework Nanoparticles: A Peroxidase-Mimicking Nanoenzyme, *Small*, 2017, **14**, 5.
31 J. Bai, C. Peng, L. Guo and M. Zhou, Metal-Organic Framework-Integrated Enzymes as Bioreactor for Enhanced Therapy against Solid Tumor via a Cascade Catalytic Reaction, *ACS Biomater. Sci. Eng.*, 2019, **5**, 6207–6215.
32 Y. Shen, X. Gao, H. Chen, Y. Wei, H. Yang and Y. Gu, Ultrathin C_3N_4 nanosheets-based oxidase-like 2D fluorescence nanozyme for dual-mode detection of organophosphorus pesticides, *J. Hazard. Mater.*, 2023, **451**, 131171.
33 Y. Shen, Y. Wei, X. Gao, C. Nie, J. Wang and Y. Wu, Engineering an enzymatic cascade catalytic smartphone-based sensor for onsite visual ratiometric fluorescence-colorimetric dual-mode detection of methyl mercaptan, *Environ. Sci. Technol.*, 2023, **57**, 1680–1691.
34 L. Luo, J. Zhuo, Y. Zhang, W. Zhang, W. Su, J. Sun, Y. Shen and J. Wang, Integrated design of a dual-mode colorimetric sensor driven by enzyme-like activity regulation strategy for ultratrace and portable detection of Hg^{2+}, *Environ. Sci. Technol.*, 2023, **57**, 13397–13407.
35 X. Zhu, X. Pang, Y. Zhang and S. Yao, Titanium carbide MXenes combined with red-emitting carbon dots as a unique turn-on fluorescent nanosensor for label-free determination of glucose, *J. Mater. Chem. B*, 2019, **7**, 7729–7735.
36 Y. Zhang, Z. Gao, W. Zhang, W. Wang, J. Chang and J. Kai, Fluorescent carbon dots as nanoprobe for determination of lidocaine hydrochloride, *Sens. Actuators, B*, 2018, **262**, 928–937.
37 J. Wang, M. K. Motlagh, M. Noroozifar, K. Kerman and H. B. KraatZ, Ferrocene-functionalized multiwalled carbon nanotubes for the simultaneous determination of dopamine, uric acid, and xanthine, *Chem. Eur.*, 2022, **3**, e202100907.